

Stress Orientations in the Fort Worth Basin, Texas, Determined from Earthquake Focal Mechanisms

by Louis Andrew Quinones, Heather R. DeShon, Maria B. Magnani, and Cliff Frohlich*

Abstract Since 2008, the Fort Worth basin (FWB) in northern Texas has experienced more than 30 M 3.0+ earthquakes, including one M 4.0. Earthquakes have primarily occurred on Precambrian basement faults and within the overlying Ellenburger limestone unit, which is the primary wastewater disposal formation used in the basin. Using data recorded by local seismic networks, we generate 240 focal mechanisms for the Azle–Reno, Irving–Dallas, and Venus sequences using P -wave first-motion and S - to P -wave (S/P) amplitude ratio data. The mechanism solutions describe primarily northeast (NE)–southwest (SW)-trending normal faults for each sequence and display a surprising lack of intersequence variability. Formal focal mechanism (FMF) stress inversions indicate maximum regional horizontal stress in the basement strikes 20° – 25° east (E) of north (N), consistent with borehole breakout data collected from the overlying sedimentary succession, suggesting that the majority of seismogenic faults in the basin are optimally oriented for failure. We show via Mohr diagrams that increases in pore-fluid pressure at fault depths, with magnitudes similar to those observed at other induced-seismicity sites, are capable of inducing slips along the causative faults of the 2013–2015 Azle–Reno, 2014–present Irving–Dallas, and 2015 Venus earthquake sequences in the FWB.

Electronic Supplement: Details about the Southern Methodist University (SMU) earthquake catalog and network coverage, figures showing the eight velocity models used for earthquake location and focal mechanism generation, parameter information for focal mechanism calculations, additional information on stress results, and the data files described in the main article.

Introduction

Numerous studies characterized and linked earthquakes in the Fort Worth basin (FWB) in Texas to wastewater disposal activities associated with shale-gas extraction (Frohlich *et al.*, 2010, 2011, 2016; Frohlich, 2012; Justinic *et al.*, 2013; Hornbach *et al.*, 2015, 2016; Walsh and Zoback, 2015; Lund Snee and Zoback, 2016; Magnani *et al.*, 2017; Scales *et al.*, 2017; Ogwari *et al.*, 2018). Large-volume wastewater injection in the basin began around 2004 (Pollastro *et al.*, 2007), and the first felt earthquakes occurred in October 2008 (e.g., Frohlich *et al.*, 2016). Wastewater is injected primarily in the Ellenburger carbonate platform, which overlies the Precambrian basement (Pollastro *et al.*, 2007). Modeling suggests that given a permeable basement fault, pore pressure perturbations caused by wastewater injection into overlying units

can propagate into the underlying basement formation (e.g., Chang and Segall, 2016), and if the pre-existing basement faults are near critical stress levels (one of the fundamental assumptions underlying many studies of induced seismicity), then these small stress perturbations can reactivate the faults (Horton, 2012; Kim, 2013; Lund Snee and Zoback, 2016).

Here, we use earthquake focal mechanisms to assess the local stress field and the orientations of the source faults for the Azle (2013–2015), Irving–Dallas (2014–present), and Venus (2015–present) earthquake sequences (Fig. 1). Each individual sequence was monitored by a local network of short-period, broadband, and strong-motion stations located within 15 km of the earthquake epicenters, and in all cases a causative fault is identified using cataloged earthquake hypocenters. We determine 240 focal mechanisms using P -wave first-motion and S - to P -wave (S/P) amplitude ratios (Hardebeck and Shearer, 2002, 2003). We then use these mechanisms to conduct single focal mechanism (FMS) and formal focal

*Also at Institute for Geophysics, Jackson School of Geosciences, University of Texas at Austin, 10100 Burnet Road (R2200), Austin, Texas 78758-4445.

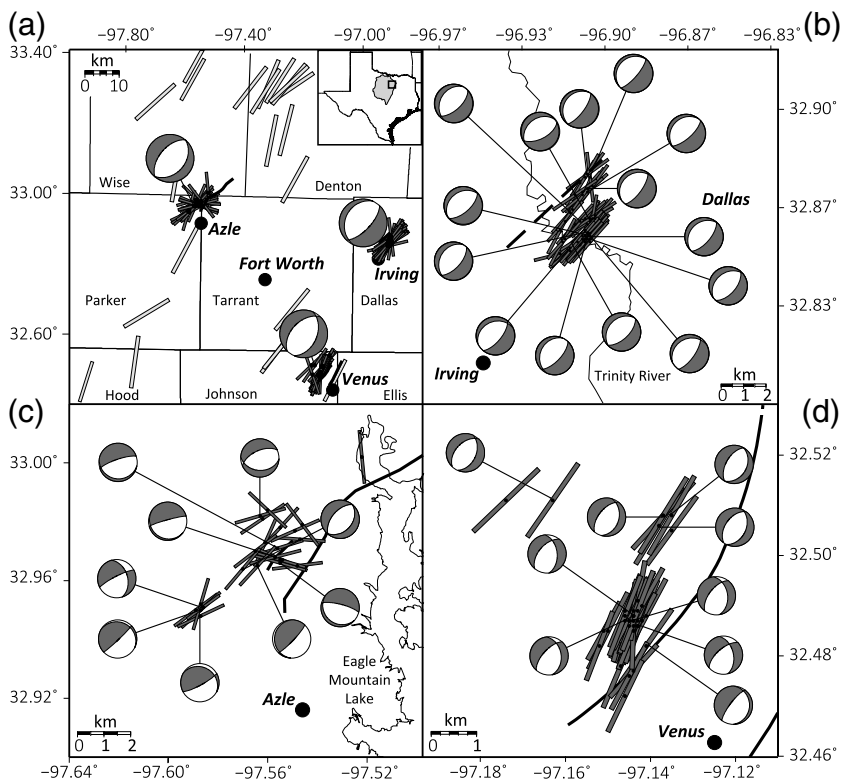


Figure 1. (a) Map view of the Fort Worth basin (FWB) showing the calculated B-axis orientations (dark gray bars) for individual earthquakes and a characteristic mechanism for each sequence. Maximum horizontal stress ($S_{H\max}$) orientations (light gray bars), calculated from borehole breakouts in the overlying sedimentary units (Lund Snee and Zoback, 2016), align with the B axes. Counties and cities discussed in the [Effective Stress Magnitude and Mohr-Coulomb Failure Analysis and Discussion](#) sections are indicated, and the inset shows the boundaries of the FWB relative to the study area (square). Zoomed views of the (b) Irving–Dallas, (c) Azle, and (d) Venus sequence areas show a sample of focal mechanisms characteristic of each sequence. For the Irving–Dallas and Venus sequences, only B axes for A and B quality mechanisms are shown. The faults (solid black lines) were mapped using a combination of Southern Methodist University catalog hypocenters and active source data (Hornbach *et al.*, 2015; Magnani *et al.*, 2017; Scales *et al.*, 2017). All faults are shown at the top of the Ellenburger.

mechanism (FMF) stress inversions, allowing us to determine the principal stress orientations in the basement. We follow the conventions of the World Stress Map Project (Barth *et al.*, 2008) and refer to principal stress orientations determined using individual focal mechanisms as FMS solutions and principal stress orientations using formal stress inversions of multiple mechanisms as FMF solutions. For each earthquake sequence, the principal stress orientations are combined with estimates of effective principal stress at seismogenic depths to determine the average pore pressure perturbation needed to induce fault slip under Mohr–Coulomb failure criteria.

Focal Mechanism Determination

The Southern Methodist University (SMU) earthquake hypocenter catalog for the FWB is derived using the GenLoc earthquake location algorithms (Pavlis *et al.*, 2004) implemented in the Antelope software system (Kinematics) and local 1D velocity models developed for each of the

individual earthquake sequences (i.e., Hornbach *et al.*, 2015; Scales *et al.*, 2017). Formal uncertainties reported as 68% confidence ellipsoids for well-recorded events have major axis and depth axis lengths of < 0.5 km. Further details regarding station geometry, earthquake location procedure, and velocity models are available in the [E](#) electronic supplement (The SMU Earthquake Catalog section; Figs. S1–S3). For focal mechanism determination, we selected only earthquakes with a minimum of six P -wave arrivals reported on three-component sensors with manually identified first motions and a signal-to-noise ratio threshold of 3. This selection reduced the 2013–2016 SMU local earthquake catalog from ~ 1300 to 240 earthquakes with a 0.1–3.8 magnitude range. We calculated takeoff angles using the HASH software suite (Hardebeck and Shearer, 2002, 2003) by incorporating the FWB velocity models as described in [E](#) The SMU Earthquake Catalog section. Because of the small magnitudes, data are primarily recorded at stations within a 15-km epicentral distance and associated with up-going ray paths.

Focal mechanisms were calculated by combining P -wave first-motion and S/P amplitude ratio data within HASH. We measured P and S amplitudes from instrument-response-corrected waveforms that were Butterworth band-pass filtered between 5 and 25 Hz. The ratio of the P -wave peak amplitude recorded on the vertical channel between 0.10 s preonset and 0.25 s postonset, and the S -wave peak amplitude between 0.20 s preonset and 1.80 s postonset, as recorded on either of the two horizontal channels, was calculated. We then corrected the observed S/P amplitude ratios for site and path effects following the procedures outlined in Shen *et al.* (1997) and Hardebeck and Shearer (2003), and that are summarized in this study. Site effects were taken to be linear, which assumes that the amplification of the seismic waves and station distance are directly related. In this study, because epicenter-to-station distances are small (< 15 km), seismic-wave attenuation is limited to the shallow crust near the receivers so that the site-effect station correction also corrects for possible path effects. The station correction was calculated as the difference between the mean observed $\log_{10}(S/P)$ value at each station and the theoretical mean $\log_{10}(S/P)$ value for a fully sampled focal sphere. Because the local networks deployed around individual earthquake sequences (Azle, Irving–Dallas, Venus) do not have any significant biases when sampling the focal sphere, the theo-

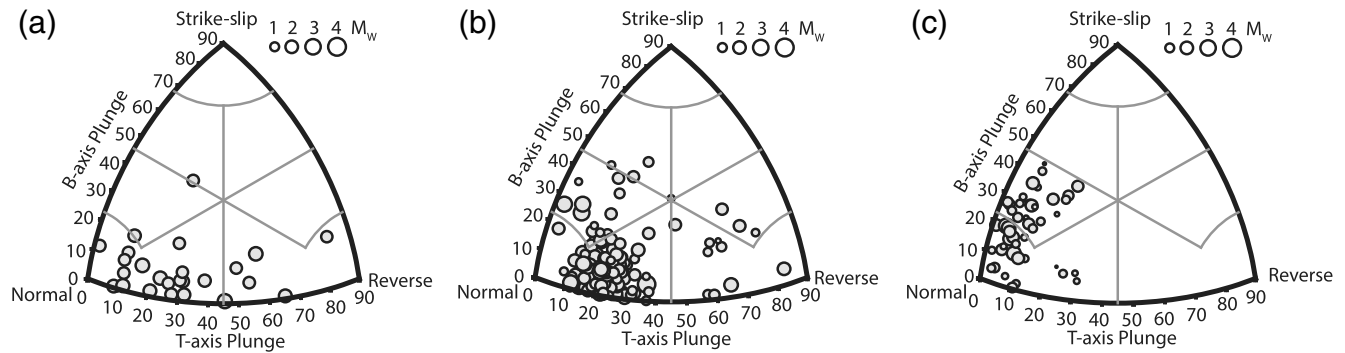


Figure 2. Ternary plots showing P, T, and B axes plunge to classify the fault type that each mechanism describes following the parameters defined by Álvarez-Gómez (2014). Each circle denotes a different mechanism solution scaled by magnitude for the (a) Azle, (b) Irving–Dallas, and (c) Venus sequences.

retical mean $\log_{10}(S/P)$ value was calculated using the overall mean $\log_{10}(S/P)$ value for each recording network.

Single Earthquake Mechanism Results

We calculated 25 focal mechanisms for the Azle sequence, 166 for the Irving–Dallas sequence, and 49 for the Venus sequence (Fig. 1) with qualities (assigned A–D) based primarily on the root mean square (rms) fault-plane uncertainty associated with each mechanism, along with other parameters outlined in the HASH manual (Hardebeck and Shearer, 2002; Table S2). Within HASH, the rms fault-plane uncertainty is calculated by taking the normal vectors of each possible fault-plane solution for a given event and solving for an average normal vector value. The rms of the differences between fault-plane solution normal vectors of individual events and the average normal vector becomes the rms fault-plane uncertainty. The best-constrained, “A” quality, mechanisms report $\leq 25^\circ$ rms fault-plane uncertainty. For the FWB data set, the 153 combined mechanisms from the Irving–Dallas and Venus sequences are primarily quality A and B grade and have an average rms fault-plane uncertainty of 26.6° . The rapid deployment and placement of seismic stations relative to the occurrence of earthquakes contributed to the overall high-quality mechanisms for these sequences. The Azle mechanisms contain more variability, which we attribute to the more complex deployment history of the Azle network (Hornbach et al., 2015). Sixteen of the twenty-five Azle mechanisms are low quality, D grade solutions with rms fault-plane uncertainties of $\geq 45^\circ$, and the average rms fault-plane uncertainty is 44.1° .

We then calculated the slip and normal vectors for each focal mechanism using the reported strike, dip, and rake from one of the nodal planes. These two vectors were then used to define the azimuth and plunge of the P (pressure), T (tension), and B (null) axes for each earthquake. For all three of the FWB sequences studied in this article, the median P-axis plunge is greater than 52° and the T-axis plunge is less than 40° , indicating that all three faults can be classified as normal faults (Fig. 2). A normal-faulting regime is consistent with seismic-reflection data that show normal faulting

associated with relocated hypocenters for the Azle (Hornbach et al., 2015), Venus (Magnani et al., 2017; Scales et al., 2017), and Irving–Dallas (Magnani et al., 2017) sequences. The nodal plane consistent with the strike and dip of the planar features in the SMU hypocenter catalog and available 2D and 3D seismic-reflection data are taken as the fault-plane solution for each earthquake. For the FWB data set, mechanisms from the Irving–Dallas and Venus sequences show a high degree of uniformity, with median fault strikes of $38.8^\circ \pm 5.4^\circ$ and $220^\circ \pm 4.4^\circ$, respectively (Fig. 2).

The P, T, and B axes derived for individual earthquakes can be used as approximations for local stress orientation. For normal faulting, the P axis should parallel the maximum vertical stress (S_V), the B axis should parallel the maximum horizontal stress ($S_{H\max}$), and the T axis should parallel the minimum horizontal stress ($S_{H\min}$). Hence, the P, T, and B axes are considered FMS stress orientations. Figure 1 shows the B-axis orientations for focal mechanisms associated with each of the three earthquake sequences. The B-axes, acting as an approximation of the $S_{H\max}$ orientation, lie almost parallel to the strikes of the northeast (NE)–southwest (SW) basement faults with orientations of $40^\circ \pm 8.1^\circ$ east (E) of north (N) for the Irving–Dallas sequence, $26^\circ \pm 5.4^\circ$ E of N for the Venus sequence, and $72.8^\circ \pm 33.3^\circ$ E of N for the Azle sequence. In the FWB, an independent estimate of $S_{H\max}$ has been reported using borehole breakout data from shallower units (Lund Snee and Zoback, 2016) and agrees well with the FMS-derived stress orientations. Hereafter, the terms S_V , $S_{H\max}$, and $S_{H\min}$ are used only when describing estimates of principle stress orientations and contain no information about magnitude.

Formal Stress Inversion Method and Results

Although the FMS-derived P, T, and B axes provide an approximation of the coseismic stress orientations for each individual earthquake, these orientations are not equivalent to documenting the full stress tensor (Michael, 1984; Lund and Townend, 2007). A formal stress inversion of the combined focal mechanism data, called the FMF solution, comes closer to approximating the full second-order stress tensor

defined by six stress parameters. Typically, these inversions can resolve only four stress parameters that mathematically define the deviatoric component of the full stress tensor: the relative magnitudes of the three principal stresses and a defined shape ratio R , in which R is a measure of the intermediate stress magnitude relative to the other principal stress magnitudes. For the FWB normal-faulting regime, we assume the shape ratio is $R = (\sigma_1 - \sigma_2)/(\sigma_1 - \sigma_3)$, in which σ_1 , σ_2 , and σ_3 are the effective maximum, intermediate, and minimum compressive stresses, respectively (Michael, 1984, 1987; Gephart and Forsyth, 1984). Hereafter, the terms σ_1 , σ_2 , and σ_3 refer to principal stress estimates that include information on both orientation and magnitude. For normal faults, the orientations of the σ_1 , σ_2 , and σ_3 principal stresses derived from FMF should be consistent with the orientations of the S_V , $S_{H_{\max}}$, and $S_{H_{\min}}$ stress orientations, respectively, derived from FMS approaches.

Lund (2000) recognized that it is possible to estimate the azimuth and plunge of the three principal stresses using the deviatoric component of a stress tensor when one of the three principals is perfectly vertical. Because the inversion of the focal mechanism data yields results even when none of the three principal stresses are perfectly vertical, we employ the methodology of Lund and Townend (2007) that mathematically estimates the principal stress orientations given an arbitrary stress tensor. Because the isotropic component of a second-order tensor by definition has no directionality, the isotropic component contains no unique information on the orientation of the stress axes. Formal stress inversions using the normal and slip vectors resulting from focal mechanism calculations (Michael, 1984) produce a partial stress tensor equivalent to only the deviatoric component of the tensor. Lund and Townend (2007) combined the partial stress tensor and shape ratio value from the FMF solutions to calculate the principal stress orientations. Similar to stress orientations from FMS methods, these FMF-derived principal stress orientations do not necessarily describe the *in situ* local stress field principal stress orientations; instead, they describe the principal stress orientations active on the seismogenic faults at the time of failure.

We employed the STRESSINVERSE software by Vavrycuk (2014), which uses an iterative least-squares version of the Michael (1984) method to solve for relative stress magnitudes, stress orientations, and shape ratios using focal mechanism data. The inversion approach does not require *a priori* determination of the true fault plane; rather, the input data are the strike, dip, and rake of both nodal planes associated with sets of earthquakes. For the FWB study, all A–B grade mechanisms for the Irving–Dallas and Venus sequences, and all A–D grade mechanisms for the Azle sequence were used. The inversion solves for the relative magnitudes and orientations of the local stress field and shape ratio, and then uses the best-fit stress field solution to identify the nodal planes optimally oriented for failure under the Mohr–Coulomb failure theory. Therefore, the inversion also solves for a preferred coefficient of sliding friction (μ) value by

examining the μ -value that maximizes fault-plane failure under the assumptions of the Mohr–Coulomb failure theory. The μ for each stress inversion was allowed to vary in the range of the standard values described by Byerlee’s law of 0.60–0.85 (Byerlee, 1978). Sensitivity tests using the FWB data indicated that the actual μ -value chosen has little effect on the calculated principal stress orientations or shape ratio value (Fig. S4).

Formal stress inversions for the Irving–Dallas and Venus sequences resulted in similar stress orientations and shape ratio values. The shape ratio R was determined to be 0.55 and 0.51 for the Irving–Dallas and Venus sequences, respectively. Therefore, the Irving–Dallas and Venus sequences occur within nearly identical normal-faulting stress regimes. Moving forward, we combined the high-quality Irving–Dallas and Venus data sets into one joint inversion to explore how stress orientations vary from E (Irving–Dallas, Venus) to W (Azle) across the FWB.

Figure 3 shows the results of 100 inversions of the Azle and joint Irving–Dallas/Venus sequences using the Michael (1987) bootstrap resampling method, along with a histogram of the resulting shape ratio values. The resulting σ_1 , σ_2 , and σ_3 orientations for the two inversions in trend/plunge format are $169^\circ/65^\circ$, $24^\circ/21^\circ$, and $289^\circ/13^\circ$ for the Azle inversion and $249^\circ/74^\circ$, $22^\circ/11^\circ$, and $115^\circ/12^\circ$ for the joint Irving–Dallas/Venus inversion (stars in Fig. 3). The larger range of σ_2 and σ_3 for Azle shown in Figure 3 reflects the greater uncertainties associated with that data set. The shape ratios were calculated to be 0.87 ± 0.02 for Azle and 0.60 ± 0.02 for Irving–Dallas/Venus. The shape ratios can be converted into the A_ϕ system, which is commonly used in the induced seismicity literature to quantify the faulting regime (Lund Snee and Zoback, 2016; Alt and Zoback, 2017). Defined by Simpson (1997), the ϕ -value is related to R as $\phi = 1 - R$. For normal-faulting regimes such as the FWB, $A_\phi = \phi$. The A_ϕ values for Azle and Irving–Dallas/Venus are 0.13 and 0.40, respectively, for which $A_\phi = 0$ is pure radial normal faulting (no strike-slip component). The Azle focal mechanism data set has larger nodal-plane uncertainties, more mechanism variability, and a small number of mechanisms (25). However, nodal-plane uncertainty is not explicitly included in the inversion. Therefore, we assume that the principal stress orientations and shape ratios have greater uncertainties than formally reported by observing the standard deviations of the bootstrap resampling, especially for Azle.

Effective Stress Magnitude and Mohr–Coulomb Failure Analysis

To assess whether pore-fluid pressure perturbations associated with wastewater injection indicate that Mohr–Coulomb fault failure has occurred, we need estimates of the effective stress magnitudes. For normal faults in the FWB, the largest principal stress (σ_1) is assumed to be the overburden pressure. Using prior geologic (Pollastro *et al.*, 2007; Vermilyen, 2011; Hornbach *et al.*, 2015; Eastman and Murin,

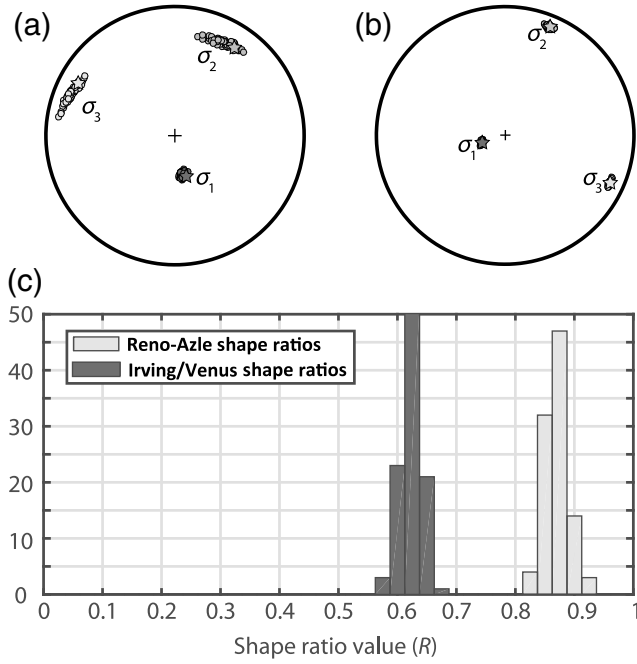


Figure 3. (a,b) Stereonet projections of the principal stress directions for the (a) Azle and (b) joint Irving–Dallas/Venus stress inversions. The dark gray, gray, and light gray dots represent the bootstrap solutions of the σ_1 , σ_2 , and σ_3 principal stresses and provide information on confidence intervals. The dark gray, gray, and light gray stars represent the best solution orientations of the principal stresses. (c) Histograms of the shape ratio R , bootstrap solutions.

2016; Magnani *et al.*, 2017) and fluid flow property (Hornbach *et al.*, 2016) studies, we estimate the densities and thicknesses of the formations and depths of the faults to calculate overburden pressure. The relationship between the maximum (σ_1) and minimum (σ_3) compressive stresses is defined by the coefficient of the sliding friction (μ) and cohesion (C) values chosen for each fault

$$2C = \sigma_1[(\mu^2 + 1)^{1/2} - \mu] - \sigma_3[(\mu^2 + 1)^{1/2} + \mu] \quad (1)$$

(Scholz, 2002). Given a lack of information about the faults prior to slip, separating the effects of cohesion from the

effects of μ is not feasible. Thus, we take cohesion to be zero and solve for σ_3

$$\sigma_3 = \sigma_1[(\mu^2 + 1)^{1/2} - \mu]/[(\mu^2 + 1)^{1/2} + \mu]. \quad (2)$$

For all three faults, we use a standard μ -value of 0.60. We use the shape ratio solutions discussed previously to solve for the intermediate stress magnitude using

$$\sigma_2 = \sigma_1 - R(\sigma_1 - \sigma_3). \quad (3)$$

The pressure gradients used to calculate the absolute overburden pressure are shown in Table 1, with a pressure gradient for the shallow sedimentary units and a gradient for the Ellenburger carbonate unit. Section thicknesses are also reported (Table 1). The overburden pressures were calculated to depths equal to the top of the seismogenic portion of the fault associated with each sequence, which are roughly equivalent to the depth of the Ellenburger–crystalline basement contact at each site. The initial absolute overburden pressures were calculated using a pore-fluid pressure (P_p) value of zero. A hydrostatic P_p gradient of 9.8 MPa/km was then subtracted from these absolute overburden pressures to calculate the effective σ_1 values for each sequence. After calculating the σ_3 and σ_2 effective stress magnitudes using equations (2) and (3), we then combine the principal effective stress magnitudes with our FMF-derived principal stress orientations to generate a full stress tensor for each sequence (Table 1). This full stress tensor is then transformed into a 3D Mohr diagram showing the relationships between the three principal stresses and associated fault-plane solutions for each sequence (Fig. 4).

To induce slip on the optimally oriented fault planes (faults striking 20°–40° NE), we find that average P_p increases of 5.25 ± 1.74 , 3.48 ± 2.39 , and 2.04 ± 2.27 MPa are needed for the Azle, Irving–Dallas, and Venus sequences, respectively. The magnitude distribution of the required change in pore pressure (ΔP_p) needed to induce slip on each of the optimally oriented fault planes is shown in (E) Figure S5. Adding these ΔP_p values to our initial hydrostatic P_p gradient yields P_p gradients of 11.55 ± 0.58 , 10.67 ± 0.60 , and

Table 1
Geologic Parameters Based on Well-Log Data of the Three Earthquake Sequences Used to Calculate the Effective Magnitudes of the Principal Stresses

	Azle	Irving–Dallas	Venus
Above Ellenburger pressure gradient (MPa/km*; psi/km†)	24.88; 3,608.5	24.88; 3,608.5	24.88; 3,608.5
Top of Ellenburger depth (km)	2.00	2.74	2.35
Ellenburger pressure gradient (MPa/km; psi/km)	25.3; 3,669.5	25.3; 3,669.5	25.3; 3,669.5
Ellenburger–basement boundary depth (km)	3.00	4.00	4.00
Seismogenic fault–depth range (km)	3–8	4–8	4–6
Absolute overburden pressure (MPa; MPa/km; psi)	75.06; 25.02; 10,866.5	100.05; 25.01; 14,511	100.21; 25.05; 14,534.2
σ_1 effective pressure (MPa; MPa/km; psi)	45.66; 15.22; 6,622.4	60.84; 15.21; 8,824.1	61.00; 15.25; 8,847.3
σ_2 effective pressure (MPa; MPa/km; psi)	18.66; 6.22; 2,706.4	36.04; 9.01; 5,227.1	36.16; 9.04; 5,244.6
σ_3 effective pressure (MPa; MPa/km; psi)	14.64; 4.88; 2,123.4	19.52; 4.88; 2,831.1	19.56; 4.89; 2,836.9

*MPa/km refers to a pressure gradient in megapascals per kilometer.

†psi/km refers to a pressure gradient in pounds per square-inch per kilometer.

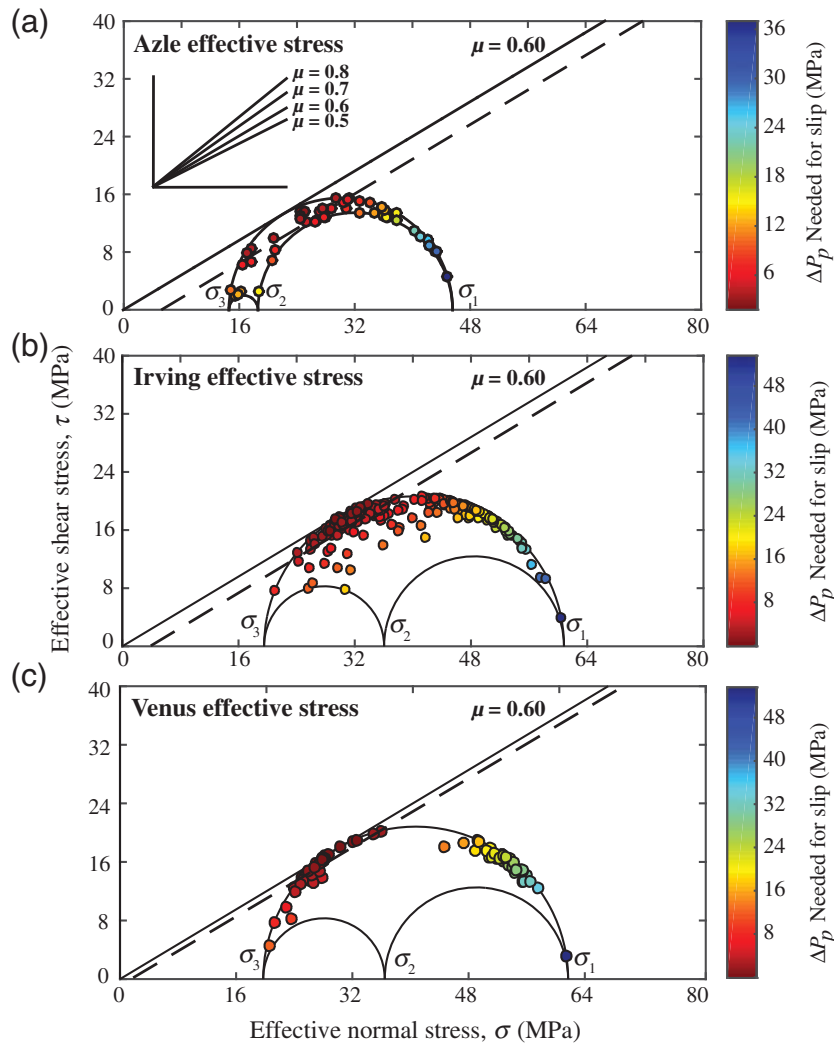


Figure 4. Mohr circle representations of the effective stresses for the (a) Azle, (b) Irving-Dallas, and (c) Venus sequences. Both nodal-plane solutions from each generated mechanism (circles) are colored by the stress change ΔP_p needed to induce slip at their respective nodal-plane orientations. For all three sequences, the left portion of the Mohr circle represents a northeast-southwest-striking nodal-plane orientation, and the right portion of the Mohr circle represents a northwest-southeast-striking nodal-plane orientation. The solid line represents the original failure criterion created using values for the friction coefficient μ of 0.6 and the cohesion C of 0. Dashed lines represent the failure criterion after it has been shifted by the average ΔP_p needed to induce slip for each sequence. The inset in (a) represents the slopes of failure criterion lines with different μ -values ranging from 0.5 to 0.8 for comparison purposes to the displayed failure criterion line for each Mohr circle.

10.31 ± 0.57 MPa/km at the Azle, Irving-Dallas, and Venus sequence sites, respectively.

These ΔP_p values were determined using effective stress magnitudes calculated assuming a μ value of 0.60 and, although the principal stress orientations are not sensitive to μ , this assumption may not be accurate for the calculated ΔP_p values. We test this sensitivity by varying μ between 0.50 and 0.85 (Fig. 5). The differences in average ΔP_p needed to induce slip at the sequence sites as μ varies from 0.50 to 0.85 are not very large (0.42, 0.48, and 0.88 MPa for the Azle, Irving-Dallas, and Venus sequences, respectively)

when compared with the overall average ΔP_p values for each sequence. For the Azle and Irving-Dallas sequences, the average ΔP_p needed to induce slip increases as the μ -value increases. The best-fit lines through the distribution of the NE-SW fault-plane orientations for these two sequences exhibit slopes closer to 0.50 than 0.85 (Fig. 4), and the average ΔP_p needed for a fault to slip reaches a minimum when these lines parallel the failure criterion set by the static parameter μ . The opposite trend is observed with the Venus data, in which the average ΔP_p needed to induce slip decreases as the μ -value increases. The NE-SW-trending fault-plane solutions from the Venus sequence are best-fit with a much steeper slope of 0.85, but the distribution of strikes and dips associated with the NE-SW nodal planes is low, leading to poor control on the slope of the best-fit line. Therefore, we conclude that the Venus result does not reflect fault strength differences with the Azle and Irving-Dallas faults as much as it reflects the lack of variability in the Venus focal mechanism data.

The P_p gradient values calculated using mechanism fault-plane solutions, earthquake-derived local stress field orientations, and estimated effective stress magnitudes are consistent with P_p increases, reported as either pressure higher than hydrostatic or pressure gradients within injection units in north Texas and Oklahoma (Sone and Zoback, 2014; Fan *et al.*, 2016; Lund Snee and Zoback, 2016; Walsh and Zoback, 2016). Borehole breakout data in the Barnett Shale near the Reno-Azle area suggested a P_p gradient value of 10.86 MPa/km (Vermylen, 2011). Previous FWB studies used P_p gradient values ranging from 9.95 to 11.76 MPa/km, with the maximum value being associated with the most overpressured parts of the

FWB in northeast Johnson County (Bowker, 2007; Sone and Zoback, 2014). Additional research into the Arbuckle formation properties in north central Oklahoma (the Arbuckle Group in Oklahoma is the stratigraphic and lithological equivalent of the Ellenburger Group in the FWB) with respect to potential fault slipping reported P_p gradients ranging from 9.20 to 10.0 MPa/km (Walsh and Zoback, 2016). Following the May 2015 M 4.0 earthquake in Venus, the Texas Railroad Commission required nearby injection wells to perform fall-off tests, and the resulting downhole pressure data indicated P_p gradients of 10.23–10.93 MPa/km within the Ellenburger (1.7–4.5 MPa higher than hydrostatic at the

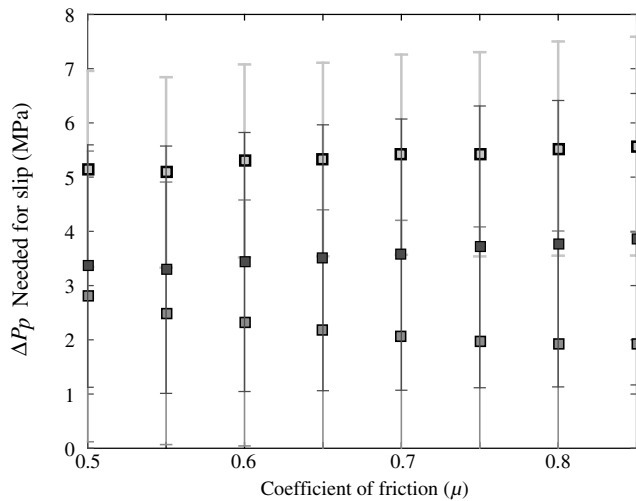


Figure 5. Plot showing the average change in the pore pressure ΔP_p needed to induce slip at the Azle (light gray), Irving–Dallas (dark gray), and Venus (gray) sequence sites using various values of the coefficient μ to calculate effective stress magnitudes.

Ellenburger–basement boundary) in northeast Johnson County (Hornbach *et al.*, 2016). Fall-off testing in the Azle area following the 2013–2014 *M* 3.5+ earthquakes also indicated that the Ellenburger was overpressured (Hornbach *et al.*, 2015).

Discussion

The well-constrained Irving–Dallas and Venus mechanism catalogs describe NE–SW-striking normal faults with very little variability in fault-plane solutions (Fig. 2b,c). Only 6% of the events near Venus and 12% of the Irving–Dallas events indicate oblique-normal, strike-slip, or thrust faulting (Fig. 2). This low variability is similar to that noted for the catalog generated from the 2009–2010 Cleburne, Texas, sequence in the FWB (Justinic *et al.*, 2013). Variability apparent in the Azle mechanisms cannot be interpreted because of the low quality of the mechanisms associated with changes in station geometry (© The SMU Earthquake Catalog section). Mechanism catalogs published for induced earthquakes in Oklahoma also show very little variability on individual fault strands, although the variability in mechanism solutions increases when examining areas outside of the immediate (< 2 km radius) area around the fault. Examples of this low variability can be seen in the Prague, Jones, Guthrie–Langston, and Pawnee earthquake sequences, which occur at shallow (< 10 km) depths similar to those in the FWB (McNamara *et al.*, 2015; Pennington and Chen, 2017). We speculate that the reason for a lack of mechanism variability in the FWB may be because thin damage zones limit off-fault failure, and the magnitudes of the events ($M_w \leq 4.0$) are not large enough to change the *in situ* stress state of the faults. The seismogenically active portions of the faults are short in length (< 20 km) (Magnani *et al.*,

2017), and the observation times are brief (2008 onward). Additionally, most active FWB faults are characterized by small offsets, even at the basement–Ellenburger contact, and their displacement history indicates long (i.e., millions of years) periods of dormancy and/or long return intervals (~60,000 years) (Magnani *et al.*, 2017).

In the FWB, the B-axis orientations in the crystalline basement are largely consistent with the $S_{H_{max}}$ orientations described by the borehole breakout data collected from the overlying sedimentary formations (Lund Snee and Zoback, 2016) (Fig. 2a). The B-axes results from the earthquakes confirm that NE–SW-striking faults in the FWB are optimally oriented for failure in the modern-day stress regime (Lund Snee and Zoback, 2016). The joint Irving–Dallas and Venus FMF-derived σ_2 orientation (22° E of N) is very similar to the median B-axis orientation of the Venus sequence (26° E of N), but there is a discrepancy between the Irving–Dallas median B-axis orientation (40° E of N) and the FMF-derived σ_2 orientation. No borehole breakout measurements are available near Irving–Dallas for comparison, and it is unclear whether the rotation in B-axis orientation reflects a true rotation in $S_{H_{max}}$ or a difference in *in situ* fault stress. $S_{H_{max}}$ orientations calculated using borehole data are very similar for the Azle and Venus areas (Lund Snee and Zoback, 2016), an observation that is also reflected in our stress inversion results for these two regions (24° E of N vs. 22° E of N).

Mohr diagrams for the three FWB earthquake sequences indicate that a P_p increase of < 4 MPa could induce slip on the causative Irving–Dallas and Venus basement faults, and a P_p increase of < 6 MPa could induce slip on the causative Azle fault. These increases in P_p are comparable to those estimated at the Snyder and Timpson, Texas, sites, which were calculated at their respective fault depths of 5 and 2.5 km and that found that P_p increases of 2.2–3.6 MPa were capable of inducing slip on the optimally oriented fault planes (Lund Snee and Zoback, 2016). This same range of increase in P_p was observed in the St. John area in northeastern British Columbia, in which surface injection pressure increases of 3 and 5 MPa were associated with induced earthquakes occurring between 1.8 and 3.7 km in depth (Horner *et al.*, 1994). However, a probabilistic assessment of the P_p increase needed to induce slip on a variety of faults in the northwestern part of Oklahoma instead found that P_p increases of 2 MPa at depths of 5–6 km would not be capable of inducing slip on the majority of mapped faults in the crystalline basement (Walsh and Zoback, 2016). Larger magnitude P_p increases that induce earthquakes associated with injection activities are rarer, but have been observed. The most notable case was the Paradox Valley seismicity. In Paradox Valley, Colorado, a P_p increase of ~17 MPa was documented to induce failure at depths of around 4.3 km (Ake *et al.*, 2005). In each case, although the actual magnitude of the P_p increase needed to induce slip varied, local injection activities were shown to be capable of producing sufficiently large P_p increases to induce slip.

Conclusions

The FWB focal mechanism catalog contains 240 solutions that describe three of the NE–SW-striking normal faults within the Precambrian crystalline basement that have been active since 2013. We decompose these mechanisms into principal P, T, and B-axes orientations to determine an approximation of the orientations of the principal stresses at depth. The B-axes orientations, interpreted in this article as approximations of the *in situ* $S_{H\max}$ orientations, are largely consistent with the $S_{H\max}$ orientations calculated from borehole breakout data taken from the overlying sedimentary succession (Lund Snee and Zoback, 2016). Inversions of the Azle and joint Irving–Dallas/Venus regions find an NE–SW-trending σ_2 orientation at each sequence site and shape ratio R -values of 0.87 and 0.60 for each respective inversion. Mohr circle analysis of the three sequences and associated fault-plane solutions suggests that these NE–SW-striking faults are optimally oriented for failure and require only small (< 6 MPa) increases in pore pressure to induce slip. These values are consistent with modeled pore-fluid pressure changes in the Ellenburger formation in this region, and are plausible when compared with the P_p increases observed in the induced seismicity sites in Oklahoma. Finally, we observe a lack of variability in fault-plane solutions generated from the FWB sequences. We hypothesize that this results from a temporally consistent local stress field during activation of small (< 20 km) fault lengths and speculate that thin damage zones associated with seismicogenic faults limit off-fault failure.

Data and Resources

Seismograms used in this study were collected as part of ongoing studies focusing on the seismicity occurring in the eastern part of the Fort Worth basin conducted by Southern Methodist University (SMU) using a combination of SMU, U.S. Geological Survey (USGS), Incorporated Research Institutions for Seismology (IRIS) Program for the Array Seismic Studies of the Continental Lithosphere (PASSCAL), and Texas Seismic Network (TexNet) instruments. Data can be obtained from the IRIS Data Management Center at www.iris.edu under Federated Digital Seismic Network codes NQ (USGS), ZW (SMU 2013+), 4F (SMU 2015+), and TX (TexNet 2016+) (last accessed February 2018).

Acknowledgments

The study was partially supported by U.S. Geological Survey (USGS) Earthquake Hazards Program Cooperative Agreements G15AC00141 and G16AC00247 to H. R. DeShon and M. B. Magnani and by the Texas Seismic Network (TexNet) program at the Bureau of Economic Geology, University of Texas. The authors thank Wayne Pennington, Jens-Erik Lund Snee, Cezar Trifu, Editor-in-Chief Thomas Pratt, and the anonymous reviewers for their constructive suggestions on this article. The authors also thank Monique Scales and Elizabeth Layton for manual identification of phase onset times and first motions of many earthquakes in the Southern Methodist University (SMU) catalog. The authors declare that they have

no real or perceived conflicts of interest. Information about the velocity models used for takeoff angle calculations, earthquake location accuracy, the SMU Fort Worth basin (FWB) focal mechanism catalog, and pressure gradient versions of Figures 4 and 5 in the main article are described in © The SMU Earthquake Catalog section, Table S1, Data Set S1, and Figures S6–S7, respectively, of the electronic supplement.

References

- Ake, J., K. Mahrer, D. O'Connell, and L. Block (2005). Deep-injection and closely monitored induced seismicity at Paradox Valley, Colorado, *Bull. Seismol. Soc. Am.* **95**, no. 2, 664–683, doi: [10.1785/0120040072](https://doi.org/10.1785/0120040072).
- Alt, R. C., II, and M. D. Zoback (2017). *In situ* stress and active faulting in Oklahoma, *Bull. Seismol. Soc. Am.* **107**, no. 1, doi: [10.1785/0120160156](https://doi.org/10.1785/0120160156).
- Álvarez-Gómez, J. A. (2014). FMC: A one-liner Python program to manage, classify and plot focal mechanisms, *Geophys. Res. Abstr.* **16**, EGU2014–10887.
- Barth, A., J. Reinecker, and O. Heidbach (2008). Stress derivation from earthquake focal mechanisms, *World Stress Map Project Guidelines*, 12 pp.
- Bowker, K. A. (2007). Barnett shale gas production, Fort Worth Basin: Issues and discussion, *AAPG Bulletin* **91**, no. 4, 523–533, doi: [10.1306/06190606018](https://doi.org/10.1306/06190606018).
- Byerlee, J. (1978). Friction of rocks, in *Rock Friction and Earthquake Prediction*, Contributions to Current Research in Geophysics (CCRG), Birkhäuser, Basel, 615–626, doi: [10.1007/978-3-0348-7182-2_4](https://doi.org/10.1007/978-3-0348-7182-2_4).
- Chang, K. W., and P. Segall (2016). Injection-induced seismicity on basement faults including poroelastic stressing, *J. Geophys. Res.* **121**, no. 4, 2708–2726, doi: [10.1002/2015JB012561](https://doi.org/10.1002/2015JB012561).
- Eastman, H. S., and T. Murin (2016). Geologic characterization of Johnson County, Texas, *NETL-TRS-17-2016*, *NETL Technical Report Series*, U.S. Department of Energy, National Energy Technology Laboratory, Morgantown, West Virginia, 68 pp.
- Fan, Z., P. Eichhubl, and J. F. W. Gale (2016). Geomechanical analysis of fluid injection and seismic fault slip for the M_w 4.8 Timpson, Texas, earthquake sequence, *J. Geophys. Res.* **121**, no. 4, 2798–2812, doi: [10.1002/2016JB012821](https://doi.org/10.1002/2016JB012821).
- Frohlich, C. (2012). Two-year survey comparing earthquake activity and injection-well locations in the Barnett Shale, Texas, *Proc. Natl. Acad. Sci. Unit. States Am.* **109**, no. 35, 13,934–13,938, doi: [10.1073/pnas.1207728109](https://doi.org/10.1073/pnas.1207728109).
- Frohlich, C., H. DeShon, B. Stump, C. Hayward, M. Hornbach, and J. I. Walter (2016). A historical review of induced earthquakes in Texas, *Seismol. Res. Lett.* **87**, no. 4, 1022–1038, doi: [10.1785/0220160016](https://doi.org/10.1785/0220160016).
- Frohlich, C., C. Hayward, B. Stump, and E. Potter (2011). The Dallas-Fort Worth earthquake sequence: October 2008 through May 2009, *Bull. Seismol. Soc. Am.* **101**, no. 1, 327–340, doi: [10.1785/0120100131](https://doi.org/10.1785/0120100131).
- Frohlich, C., E. Potter, C. Hayward, and B. Stump (2010). Dallas-Fort Worth earthquakes coincident with activity associated with natural gas production, *The Leading Edge* **29**, 270–275, doi: [10.1785/0120100131](https://doi.org/10.1785/0120100131).
- Gephart, J. W., and D. W. Forsyth (1984). An improved method for determining the regional stress tensor using earthquake focal mechanism data: Application to the San Fernando earthquake sequence, *J. Geophys. Res.* **89**, no. B11, 9305–9320, doi: [10.1029/JB089iB11p09305](https://doi.org/10.1029/JB089iB11p09305).
- Hardebeck, J. L., and P. M. Shearer (2002). A new method for determining first-motion focal mechanisms, *Bull. Seismol. Soc. Am.* **92**, no. 6, 2264–2276, doi: [10.1785/0120010200](https://doi.org/10.1785/0120010200).
- Hardebeck, J. L., and P. M. Shearer (2003). Using S/P amplitude ratios to constrain the focal mechanisms of small earthquakes, *Bull. Seismol. Soc. Am.* **93**, no. 6, 2434–2444, doi: [10.1785/0120020236](https://doi.org/10.1785/0120020236).
- Hornbach, M. J., H. R. DeShon, W. L. Ellsworth, B. W. Stump, C. Hayward, C. Frohlich, H. R. Oldham, J. E. Olson, M. B. Magnani, C. Brokaw, et al. (2015). Causal factors for seismicity near Azle, Texas, *Nature Comm.* **6**, doi: [10.1038/ncomms7728](https://doi.org/10.1038/ncomms7728).
- Hornbach, M. J., M. Jones, M. Scales, H. R. DeShon, M. B. Magnani, C. Frohlich, B. Stump, C. Hayward, and M. Layton (2016). Ellenburger

- wastewater injection and seismicity in North Texas, *Phys. Earth Planet. In.* **261**, 54–68, doi: [10.1016/j.pepi.2016.06.012](https://doi.org/10.1016/j.pepi.2016.06.012).
- Horner, R. B., J. E. Barclay, and J. M. MacRae (1994). Earthquakes and hydrocarbon production in the Fort St. John area of northeastern British Columbia, *Can. J. Explor. Geophys.* **30**, no. 1, 39–50.
- Horton, S. (2012). Disposal of hydrofracking waste water fluid by injection into subsurface aquifers triggers earthquake swarm in central Arkansas with potential for damaging earthquake, *Seismol. Res. Lett.* **83**, no. 2, 250–260, doi: [10.1785/gssrl.83.2.250](https://doi.org/10.1785/gssrl.83.2.250).
- Justinic, A. H., B. Stump, C. Hayward, and C. Frohlich (2013). Analysis of the Cleburne, Texas, earthquake sequence from June 2009 to June 2010, *Bull. Seismol. Soc. Am.* **103**, no. 6, 3083–3093, doi: [10.1785/0120120336](https://doi.org/10.1785/0120120336).
- Kim, W. Y. (2013). Induced seismicity associated with fluid injection into a deep well in Youngstown, Ohio, *J. Geophys. Res.* **118**, no. 7, 3506–3518, doi: [10.1002/jgrb.50247](https://doi.org/10.1002/jgrb.50247).
- Lund, B. (2000). Crustal stress studies using microearthquakes and boreholes, *Ph.D. Thesis*, Uppsala University, Sweden.
- Lund, B., and J. Townend (2007). Calculating horizontal stress orientations with full or partial knowledge of the tectonic stress tensor, *Geophys. J. Int.* **170**, no. 3, 1328–1335, doi: [10.1111/j.1365-246X.2007.03468.x](https://doi.org/10.1111/j.1365-246X.2007.03468.x).
- Lund Snee, J.-E., and M. D. Zoback (2016). State of stress in Texas: Implications for induced seismicity, *Geophys. Res. Lett.* **43**, no. 19, doi: [10.1002/2016GL070974](https://doi.org/10.1002/2016GL070974).
- Magnani, M. B., M. L. Blanpied, H. R. DeShon, and M. J. Hornbach (2017). Discriminating between natural vs. induced seismicity from long-term deformation history of intraplate faults, *Sci. Adv.* **3**, no. 11, doi: [10.1126/sciadv.1701593](https://doi.org/10.1126/sciadv.1701593).
- McNamara, D. E., H. M. Benz, R. B. Herrmann, E. A. Bergman, P. Earle, A. Holland, R. Baldwin, and A. Gassner (2015). Earthquake hypocenters and focal mechanisms in central Oklahoma reveal a complex system of reactivated subsurface strike-slip faulting, *Geophys. Res. Lett.* **42**, no. 8, 2742–2749, doi: [10.1002/2014GL062730](https://doi.org/10.1002/2014GL062730).
- Michael, A. J. (1984). Determination of stress from slip data: Faults and folds, *J. Geophys. Res.* **89**, no. B13, 11,517–11,526, doi: [10.1029/JB089iB13p11517](https://doi.org/10.1029/JB089iB13p11517).
- Michael, A. J. (1987). Use of focal mechanisms to determine stress: A control study, *J. Geophys. Res.* **92**, no. B1, 357–368, doi: [10.1029/JB092iB01p00357](https://doi.org/10.1029/JB092iB01p00357).
- Ogware, P. O., H. R. De Shon, and M. J. Hornbach (2018). The Dallas-Fort-Worth airport earthquake sequence: Seismicity beyond injection period, *J. Geophys. Res.* **123**, doi: [10.1002/2017JB015003](https://doi.org/10.1002/2017JB015003).
- Pavlis, G. L., F. Vernon, D. Harvey, and D. Quinlan (2004). The generalized earthquake-location (GENLOC) package: An earthquake-location library, *Comput. Geosci.* **30**, nos. 9/10, 1079–1091, doi: [10.1016/j.cageo.2004.06.010](https://doi.org/10.1016/j.cageo.2004.06.010).
- Pennington, C., and X. Chen (2017). Coulomb stress interactions during the M_w 5.8 Pawnee sequence, *Seismol. Res. Lett.* **88**, no. 4, 1024–1031, doi: [10.1785/0220170011](https://doi.org/10.1785/0220170011).
- Pollastro, R. M., D. M. Jarvie, R. J. Hill, and C. W. Adams (2007). Geologic framework of the Mississippian Barnett Shale, Barnett-Paleozoic total petroleum system, Bend Arch-Fort Worth Basin, Texas, *AAPG Bulletin* **91**, no. 4, 405–436, doi: [10.1306/10300606008](https://doi.org/10.1306/10300606008).
- Scales, M., H. R. DeShon, M. B. Magnani, J. I. Walter, L. Quinones, T. L. Pratt, and M. J. Hornbach (2017). A decade of induced slip on the causative fault of the 2015 M_w 4.0 Venus earthquake, northeast Johnson County, Texas, *J. Geophys. Res.* **122**, 7879–7894, doi: [10.1002/2017JB014460](https://doi.org/10.1002/2017JB014460).
- Scholz, C. H. (2002). *The Mechanics of Earthquakes and Faulting*, Second Ed., Cambridge University Press, New York, New York.
- Shen, Y., D. W. Forsyth, J. Conder, and L. M. Dorman (1997). Investigation of microearthquake activity following an intraplate teleseismic swarm on the west flank of the southern East Pacific Rise, *J. Geophys. Res.* **102**, no. B1, 459–475, doi: [10.1029/96JB02852](https://doi.org/10.1029/96JB02852).
- Simpson, R. W. (1997). Quantifying Anderson's fault types, *J. Geophys. Res.* **102**, no. B8, 17,909–17,919, doi: [10.1029/97JB01274](https://doi.org/10.1029/97JB01274).
- Sone, H., and M. D. Zoback (2014). Viscous relaxation model for predicting least principal stress magnitudes in sedimentary rocks, *J. Petrol. Sci. Eng.* **124**, 416–431, doi: [10.1016/j.petrol.2014.09.022](https://doi.org/10.1016/j.petrol.2014.09.022).
- Vavrycuk, V. (2014). Iterative joint inversion for stress and fault orientations from focal mechanisms, *Geophys. J. Int.* **199**, no. 1, 69–77, doi: [10.1093/gji/ggu224](https://doi.org/10.1093/gji/ggu224).
- Vermilyen, J. P. (2011). Geomechanical studies of the Barnett Shale, Texas, USA, *Ph.D. Thesis*, Stanford University, Stanford, Calif., 143 pp.
- Walsh, F. R., and M. D. Zoback (2015). Oklahoma's recent earthquakes and saltwater disposal, *Sci. Adv.* **1**, no. 5, doi: [10.1126/sciadv.1500195](https://doi.org/10.1126/sciadv.1500195).
- Walsh, F. R., and M. D. Zoback (2016). Probabilistic assessment of potential fault slip related to injection-induced earthquakes: Application to north central Oklahoma, USA, *Geology* **44**, no. 12, 991–994, doi: [10.1130/G38275.1](https://doi.org/10.1130/G38275.1).

Huffington Department of Earth Sciences
Southern Methodist University
P.O. Box 750395
Dallas, Texas 75275-0395
lquinones@smu.edu

Manuscript received 13 November 2017;
Published Online 10 April 2018